Journal of Materials Chemistry A

Kinetically Stable Anode Interface for Li3YCl6-Based All-Solid-State Lithium Batteries

Journal:	*Journal of Materials Chemistry A*
Manuscript ID	TA-ART-04-2021-003042.R1
Article Type:	Paper
Date Submitted by the Author:	02-Jun-2021
Complete List of Authors:	Ji, Weixiao; University of Wisconsin-Milwaukee, Mechanical Engineering Zheng, Dong; University of Wisconsin Milwaukee, Mechanical Engineering Zhang, Xiaoxiao; University of Wisconsin Milwaukee, Mechancial Ding, Tianyao; University of Wisconsin Milwaukee, Mechanical Engineering Qu, Deyang; University of Wisconsin-Milwaukee, Mechanical Engineering

ARTICLE Journal Name

Kinetically Stable Anode Interface for Li_3YCl_6-Based All-Solid-State Lithium Batteries

Received 00th January 20xx,
Accepted 00th January 20xx

DOI: 10.1039/x0xx00000x

Weixiao Ji,[‡a] Dong Zheng,[‡a] Xiaoxiao Zhang,[a] Tianyao Ding,[a] and Deyang Qu*[a]

Despite excellent ionic conductivity and electrochemical oxidative stability, the emerging halide-based solid electrolytes suffer from inherent instability toward Li metal anode. A thick and resistive interface can be formed by continuous reaction between halide electrolytes and Li anode, rendering high impedance, low Coulombic efficiency, and even short circuit of solid-state cells. Here, we report a thin argyrodite (Li_6PS_5Cl) protection layer to avoid the direct physical contact of Li anode from Li_3YCl_6, a representative halide electrolyte. Li_6PS_5Cl is kinetically stable with lithium and can also form good hetero contact with Li_3YCl_6. Highly stable Li plating/stripping cycling of symmetric cell with a steady overpotential of 100 mV after 1000 h was demonstrated, compared to severe overpotential build-up to reach 1500 mV after 60 h of the control group. Besides, $LiNi_{0.8}Co_{0.1}Mn_{0.1}O_2$/Li full solid-state cell displayed a high initial Coulombic efficiency of >87% and a stable lifetime over 100 cycles. The facile protection of Li_6PS_5Cl provides a universal way to prevent unfavorable interaction at anode interface and realizing high performance all-solid-state Li-metal batteries.

1. Introduction

All-solid-state lithium batteries (ASSLBs), by employing ceramic solid electrolyte and metallic lithium anode, is regarded as a promising alternative for the existing lithium-ion batteries (LIBs).[1-3] Due to the absence of flammable liquid electrolytes, ASSLBs can overcome the unsurmountable safety-related barrier of commercial LIBs. Also, a higher energy density can be expected of ASSLBs owing to a better stacking of cell units and the deployment of Li-metal anode.[4] Among numerous Li-ion-conducting materials, sulfides[5-7] and oxides[8,9] are the most widely explored solid electrolyte (SE) candidates. Sulfides possess high ionic conductivity, comparable to traditional liquid electrolytes. Also, the soft mechanical properties of sulfides allow for a scalable pressing-based fabrication protocol. However, these virtues are counteracted with the poor chemical stability of sulfides in humid air and moreover, the electrochemical incompatibility with conventional 4V-class cathodes. Oxides, on the other hand, possess relatively wide electrochemical stability window and acceptable chemical stability. Nevertheless, the oxides are brittle and readily suffer from mechanical damage at the interface. Furthermore, a high-temperature sintering process is often indispensable when integrating oxides into devices, which is economically impractical and poses challenge for large-scale manufacturing.[10] To this end, it is crucial to exploiting plausible electrolytes with competitive ionic conductivity, deformability, and (electro)chemical stability.[11-14]

A new family of halide-based electrolytes, with a general form of Li_3MX_6 (M=In, Y, Sc, Er, etc, X=Cl, Br, etc), have attracted ever-rising interest lately and are expected to be a possible game changer for ASSLBs.[15-17] As shown in Fig. 1, halides exhibit combined advantages of sulfides and oxides, including easy processability[18] and (electro)chemical stability toward high-voltage cathodes[19,20]. However, the poor reduction stability of halides in contact with lithium metal remains an open challenge. Interestingly, strategies to tackle the interfacial issue has been rarely reported, except for adopting Li-Y alloys (Y=In, Sn, Ge) or metallic In to replace Li metal as anode, which sacrifices the cell overall energy density by lowering the operating potential.[21,22] Recently, Riegger[23] and Fu[24] have successfully unravelled the mechanism of interplay between halides and lithium by analysing the decomposition products at the anode interface. The presence of high-valence metal cations (M^{3+}) in halides can be readily reduced to M^0 once contact with Li metal. The formed interface is electrically conductive and will keep fast growing by continuous consuming Li_3MX_6 and lithium metal, until either one is depleted or inducing a short circuit of ASSLB over time. Inspired by the vital role interfacial decomposition components played, we envisioned an ionic-conducting and Li compatible protection layer to block the unfavourable interaction between halides and Li metal.

In this Contribution, we report the construction of a kinetically stable interface by inserting an argyrodite buffer layer between Li metal and Li_3YCl_6 layer, a representative halide electrolyte. Argyrodite (Li_6PS_5Cl) was selected due to its fast ionic conduction, soft mechanical property, and more importantly, its ability to produce a kinetically stable interface in contact with Li metal.[25-27] We demonstrate Li/Li symmetric cell with a polarization potential as low as 100 mV and a stable plating/stripping behaviour over 1000 h at 0.2 mA cm^{-2}, 0.2 mAh cm^{-2}. Moreover, $LiNi_{0.8}Co_{0.1}Mn_{0.1}O_2$/Li full solid-state cell delivers a record-breaking high initial Coulombic efficiency of > 87%. To the best of our knowledge, this is the first case to employ Li metal as anode in halide-based all-solid-state batteries.

[a] *Department of Mechanical Engineering, University of Wisconsin Milwaukee, Milwaukee, WI 53211, USA. E-mail: qud@uwm.edu*

† Electronic Supplementary Information (ESI) available. See DOI: 10.1039/x0xx00000x

‡ These authors contributed equally.

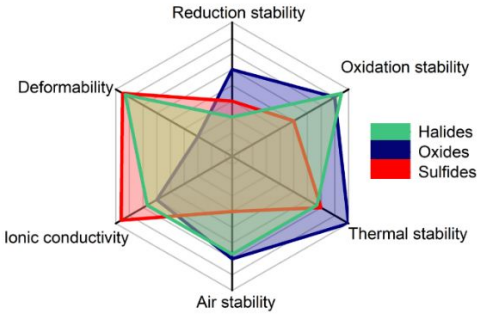

Fig. 1. Comparison of various properties among three typical families of ceramic solid electrolytes.

2. Experimental

The synthesis and processing of solid electrolytes and the electrochemical characterizations of all-solid-state cells were all conducted in Ar-filled glovebox with H_2O and O_2 levels below 0.1 ppm at 25 °C. An anti-static air ionizer (Static Care, Amazon, USA) was adopted for static removal inside glovebox. 45 µm Li foil was achieved from China Energy Lithium Co., Ltd. Li_6PS_5Cl was purchased from NEI Corp. (USA) and used as achieved. Carbon nanofibers (D × L 100 nm × 20-200 µm) was purchased from Sigma Aldrich (USA).

2.1 Synthesis of Li_3YCl_6 solid electrolyte

Lithium chloride (LiCl, Alfa Aesar, 99.9%) and yttrium chloride (YCl_3, Alfa Aesar, 99.999%) were used as received. The starting materials were firstly weighed to the stoichiometric molar ratio (1g LiCl, 1.69 g YCl_3) and hand-mixed for 10 min in an agate mortar. Subsequently, the precursors were loaded into an 80 mL milling bowl with zirconia milling balls inside (φ=5 mm). The mechanochemical reaction was carried out using a planetary micro mill (Pulverisette 7, Fritsch). The milling procedures have totally 198 cycles, with each cycle consisting of a 5 min milling step followed by a 15 min rest. A reverse mode was used to avoid the generation of local hot spots during milling. After every 99 cycles, the bowl was opened inside glovebox and the hard precursor layer was removed from the wall using a spatula. This process would re-homogenize the mixture to achieve a full powder-volume before undergoing further mechanical collision. Afterward, the powder was vacuum sealed into a glass tube at ~ 10 MPa and placed into a preheated furnace at 550 °C for 5 min. The crystallized sample was air-quenched and ready to use.

2.2 All-solid-state cell assembly

The home-made die mold is consisted of two Cr12MoV-type stainless steel plungers (diameter: 0.495 inch) and one polyether ether ketone (PEEK) tube (inner diameter: 0.5 inch). A pressure calibration kit (EQ-LC-KIT-5, MTI Corp.) was used to precisely control the stack pressure (Fig. S1). 100 mg LYCl powder was firstly loaded into the die and compacted under 275 MPa for 1 min using a hydraulic press (YLJ-15T, MTI Corp). After pressing, the residual LYCl powder on the inner wall of PEEK tube was cleaned up with a brush to avoid unnecessary contamination. For symmetric cell assembly, 10 mg, 15 mg, or 25 mg LPSCl powder were spread on each side of LYCl pallet and pressed under 375 MPa for 3 min. Then, two lithium discs (1.13 cm^2) were attached on both sides of LPSCl/LYCl/LPSCl pallet and pressed under 120 MPa for 15 s. The symmetric cells were cycled under a constant pressure of ~5 MPa. For full cell assembly, the cathode composite was made by hand grinding NMC-811, LYCl, and carbon nanofibers, with a weight ratio of 30:60:10 or 70:25:5 in an agate mortar for 5 min. Then, 20 mg cathode composite was loaded on one side of LYCl pallet and pressed under 300 MPa for 1 min. 25 mg LPSCl powder was spread on the other side of LYCl pallet and pressed under 370 MPa for 3 min. Finally, one lithium disc (1.13 cm^2) was pressed on either LYCl or LPSCl side under 120 MPa for 15 s. The Li/LPSCl/LYCl/NCM-811 cell or Li/LYCl/NCM-811 cell was cycled under a constant pressure of ~5 MPa.

2.3 Material characterization and electrochemical measurements

As shown in Fig. S2, the thickness of composite cathode, LYCl, and LPSCl layer were measured by a digital thickness gage (0.001 mm, ID-C112EXBS, Mitutoyo Corp.). The density of LYCl and LPSCl after cold press is calculated to be 1.8 g cm^{-3} and 3.5 g cm^{-3}, respectively. Scanning electron microscopy (SEM) and energy-dispersive X-ray spectroscopy (EDS) were performed on a Hitachi S-4800 field emission SEM equipped with a Bruker EDS detector. Powder X-ray diffraction (XRD) was performed on a Bruker D8 DISCOVER diffractometer with Cu Kα radiation. A low background air-tight dome sample holder (Bruker) was adopted to mount XRD powder samples. The ionic conductivities of LPSCl pallet, LYCl pallet, and LPSCl/LYCl/LPSCl pallet were measured by AC impedance spectroscopy using PARSTAT® 2273 electrochemical workstation (Princeton applied research Co. Ltd, USA) at 25 °C. The measurements were conducted under 370 MPa from 2 MHz to 1 Hz with an excitation amplitude of 10 mV. The EIS tests of symmetric cells and full cells were tested in a frequency range from 2 MHz to 0.1 Hz at 25 °C. The cyclic voltammetry (CV) measurement was conducted on an electrochemical workstation (CHI660A, USA). The galvanostatic cycling studies was carried out on Land test systems at 25 °C (CT2001A, Wuhan, China).

3. Results and discussion

3.1 The interplay between Li metal and Li_3YCl_6

Li_3YCl_6 (LYCl) was selected as a representative halide electrolyte, with a theoretical predicted cathodic limit of 0.62 V vs. Li^+/Li.[20] To analyse the reaction products at the Li/LYCl interface, Li pieces and the as-synthesized white LYCl powder were hand-ground at a molar ratio of 3:1 (Fig. 2a), according to the idealized net reaction equation $Li_3YCl_6 + 3Li \rightarrow 6LiCl + Y^0$. After 20 minutes of grinding, the reaction product turned out to be black powder and the shiny lithium pieces became completely consumed (Fig. 2b). The corresponding X-ray diffraction (XRD) patterns are shown in Fig. 2c. Strong diffraction peaks attributed to LiCl were detected as labelled. The signal of

yttrium metal is not significant, mainly caused by the low volume fraction of Y^0 compared to LiCl. In addition, Y^0 can

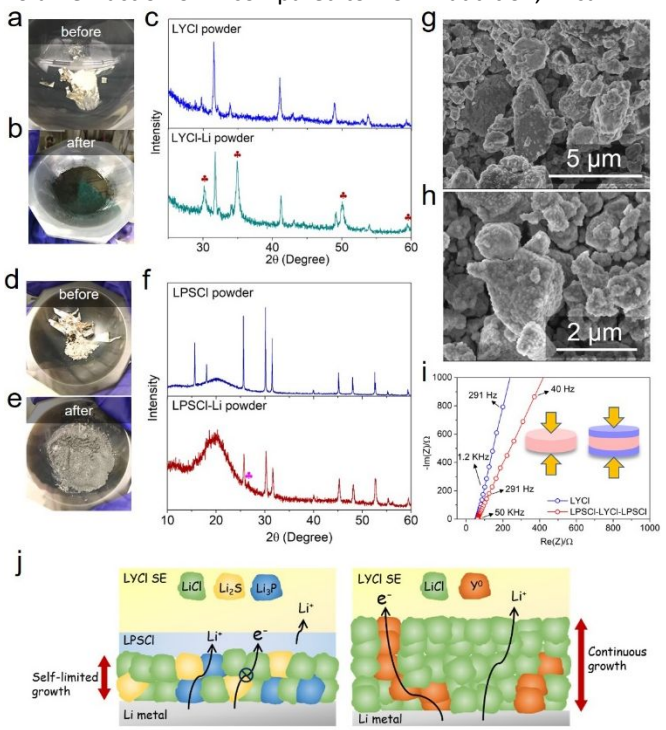

Fig. 2. Pictures of Li metal pieces and LYCl powder a) before and b) after hand grinding; c) corresponding XRD patterns of the reaction products. Pictures of Li metal pieces and LPSCl powder d) before and e) after grinding; f) corresponding XRD patterns of the reaction products. SEM images of g) LPSCl and h) LYCl powder. i) Ionic conductivity measurement of LYCl pallet and LPSCl/LYCl/LPSCl composite pallet at room temperature. j) Schematic illustration showing the Li/LPSCl/LYCl design (left) and Li/LYCl design (right).

immediately react with other species to form Y_2O_3 or $Y_2(CO_3)_2$ species.[23] Therefore, a fast-growing and mixed ion/electron conducting interface is formed one way or another. Similarly, the reaction products at the Li_6PS_5Cl/Li interface were investigated by mixing Li_6PS_5Cl (LPSCl) powder and Li pieces at a molar ratio 1:8 (Fig. 2d), according to the net interfacial reaction $Li_6PS_5Cl + 8Li \rightarrow 5Li_2S + Li_3P + LiCl$.[28] Lithium residues can still be observed from the greyish reaction products after 20 minutes (Fig. 2e). The XRD pattern (Fig. 2f) generally remain unchanged with only one additional peak assigned to Li_2S as labelled. The signal is rather weak, implying the reaction is self-limited and the reaction layer is rather thin. The dominant decomposition product, Li_2S, is an ionic conductor with low electronic conductivity, leading to a formation of a resistive interfacial layer. Regarding the other two decomposition products, Li_3P is a fast Li-ion conductor (~10^{-4} S cm^{-1}) and LiCl is less ionic conductive. Importantly, LiCl displays high interface energy against lithium, which can significantly suppress dendrite growth, same as the role LiF played in previous studies.[29-31] Overall, a kinetically stable and ionic conducting interface can be expected between Li and LPSCl, just like the SEI layer formed in liquid electrolytes.

Apart from the LPSCl/Li interface, the hetero contact at the LPSCl/LYCl interface was also investigated. SEM images shown in Fig. 2g-h displayed a similar particle size (several microns) of LPSCl and LYCl powders. The ionic conductivity measurement in Fig. 2i shows barely changed intercepts between LYCl pallet and LPSCl/LYCl/LPSCl pallet at room temperature. All these implied a favoured charge transfer process at the LYCl/LPSCl interface. A high chemical compatibility between LPSCl and LYCl was verified by monitoring the ionic conductivity evolution of well mixed LPSCl/LYCl powder with time (Fig. S3). As illustrated in Fig. 2j, the designed Li/LPSCl/LYCl structure (left) and the pristine Li/LYCl structure (right) is compared. The mixed-conducting nature of Li/LYCl interface will result in a very thick SEI formation, while a primarily ionic conducting nature of Li/LPSCl interface can generate a self-limiting SEI layer with moderate thickness.

3.2 Evaluation on the stability of anode interface in symmetric cells

To verify the feasibility of LPSCl buffer layer, Li plating/stripping behaviour of symmetric cell was measured under various conditions. Long-cycling protocol is carried out to study the accumulative effect at the interface during long-term operation (Fig. 3a). Li/LYCl/Li cell (control group) displayed an initial overpotential of ~600 mV and reach ~1500 mV after 60 h at a current of 0.2 mA cm^{-2} and capacity of 0.2 mAh cm^{-2}. The increased polarization indicated a build-up of reaction products that hinder the charge transfer at the Li/LYCl interface.[32,33] Shorting was not observed throughout the process, since the as-formed thick and dense interlayer can act as a mechanical barrier to prevent lithium creeping through SE pallet.[34] The electrochemical impedance spectra (EIS) evolution was also monitored during steady state (without charge/discharge) and after cycling (Fig. 3b). Typically, the high frequency region indicates the bulk conduction of SE while the low frequency region stands for the Li/SE interface.[35] The overall impedance only increased slightly during rest, maybe attributed to the presence of a native contamination layer (composed of impurities like insulating Li_2O, Li_2CO_3, etc.) on lithium surface.[36] After cycling, the bulk contribution did not vary significantly while the resistance assigned to the interface dramatically increased to ~32000 ohms, more than three times higher compared to the steady state. After dissembling the cell, black reaction spots and cracks can be observed unevenly distributed on the lithium substrate. The fast interface evolution and the propagation of cracks are the primary cause for chemomechanical degradation and impedance increase.[37] Fig. 3c shows the cycling performance of Li/LPSCl/LYCl/LPSCl/Li symmetric cell at the same testing condition. 25 mg LPSCl is screened out for the following study since it offers the best protection (Fig. S4). The Li plating/stripping slightly increased from 50 mV to 100 mV over 1000 h (Fig. 3d). Table S1 summarized the previously reported performance of halide-based symmetric cells and our work is one of the best. As shown in Fig. 3e, the corresponding impedance increased from 374 ohms to 379 ohms after cycling for 60 h, implying a formation of stable SEI layer and the layer would not cause a too high interface impedance.

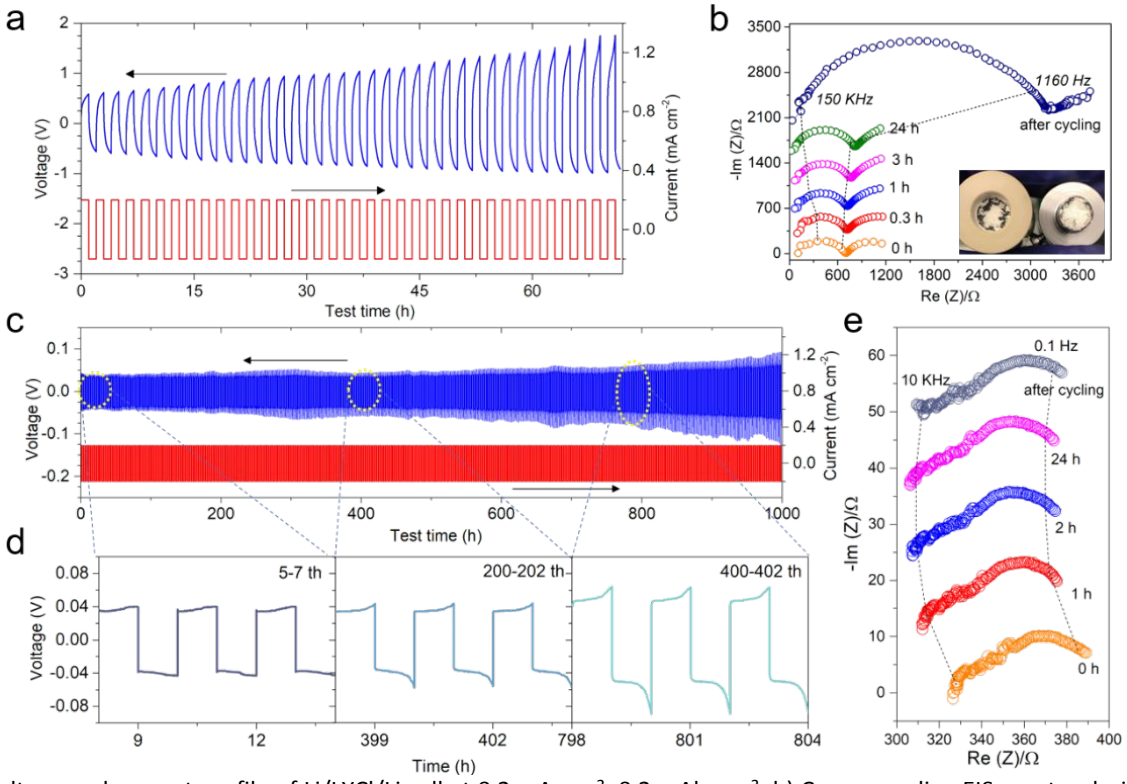

Fig. 3. a) Voltage and current profile of Li/LYCl/Li cell at 0.2 mA cm^{-2}, 0.2 mAh cm^{-2}. b) Corresponding EIS spectra during rest and after 60 h cycling. c) Voltage and current profile of Li/LPSCl/LYCl/LPSCl/Li cell at 0.2 mA cm^{-2}, 0.2 mAh cm^{-2}; d) the details indicated by the areas marked by the yellow dashes. e) Corresponding EIS spectra during rest and after 60 h cycling.

As shown in Fig. 4a, Li/LPSCl/LYCl/LPSCl/Li symmetric cell was tested with an increased capacity while the current fixing at 0.2 mA cm^{-2}. The maximum stripping capacity the cell can sustain is 1.4 mAh cm^{-2}, representing 16 % utilization of the Li electrode (theoretical capacity is 9 mAh cm^{-2}). Usually, the electrode overpotential is closely related to the changes of contact area during Li stripping process. The pore formation is the root cause for the interface deterioration under such practical conditions. Fig. 4b displayed voltage profiles of symmetric cell tested with an increasing current density but fixing at a capacity of 0.2 mAh cm^{-2}. The critical current is determined to be 0.8 mA cm^{-2}. According to former study, the overall current to avoid voids/dendrite formation for a Li/LPSCl/Li cell is 0.2 mA cm^{-2} at 3 MPa and rise to 1.0 mA cm^{-2} at 7 MPa.[38] The critical current can be highly dependent on the external stack pressure. In our case, the threshold value of Li/LPSCl/LYCl/LPSCl/Li cell is 0.8 mA cm^{-2} at 4.4 MPa, consistent with former study.

3.3 Evaluation of halide-based solid-state full cells

The high oxidation stability of halide SEs allows the use of commercial 4V-class $LiMO_2$ (M=Ni, Co, Mn, Al) cathodes without any protective coating layer. To investigate full cell performance, cathode composite was made by hand grinding LYCl SE, bare $LiNi_{0.8}Co_{0.1}Mn_{0.1}O_2$ (NCM-811) powder, and conductive carbon at a weight ratio of 60:30:10. The charge/discharge voltage profiles of NCM-811/LYCl/Li full cell and NCM-811/LYCl/LPSCl/Li full cell were compared in Fig. 5a-b. The current density is 0.1 mA cm^{-2} and the loading of NMC-811 is 6 mg cm^{-2}. At the initial cycle, NCM-811/LYCl/Li full cell exhibited a high charging capacity of 255 mAh g^{-1} and a low Coulombic efficiency (CE) of 65%. In the following cycles, the electrochemical polarization continuously increased. At the 12th cycle, the charging curve showed a long voltage plateau at 4.05 V and failed to reach the upper cutoff voltage of 4.3 V. This could be caused by continuous reaction between freshly deposited lithium and LYCl during delithiation process. By contrast, the NMC-811/LYCl/LPSCl/Li full cell delivered a capacity of 181 mAh g^{-1} and 183 mAh g^{-1} for the first two cycles, with a CE of 87% and 98%, respectively (Fig. 5b). As marked in the blue circle, no additional slope occurs prior to reaching the charge plateau, indicating no formation of space charge layer at the NCM-811/LYCl interface. A higher active material content leads to an even higher ICE of 89% (Fig. S5). Typical curves representing

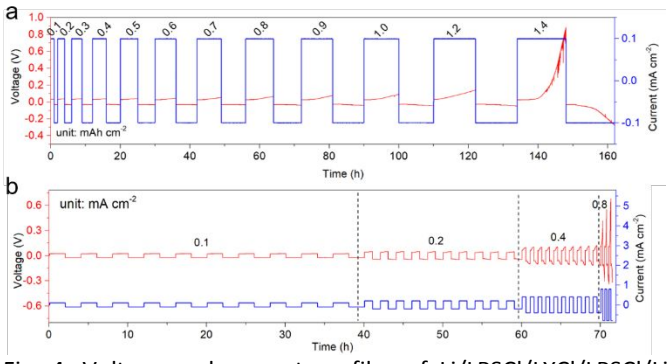

Fig. 4. Voltage and current profiles of Li/LPSCl/LYCl/LPSCl/Li symmetric cell a) at increased capacities with a constant current of 0.2 mA cm^{-2} and b) at increased current densities with a constant capacity of 0.2 mAh cm^{-2}.

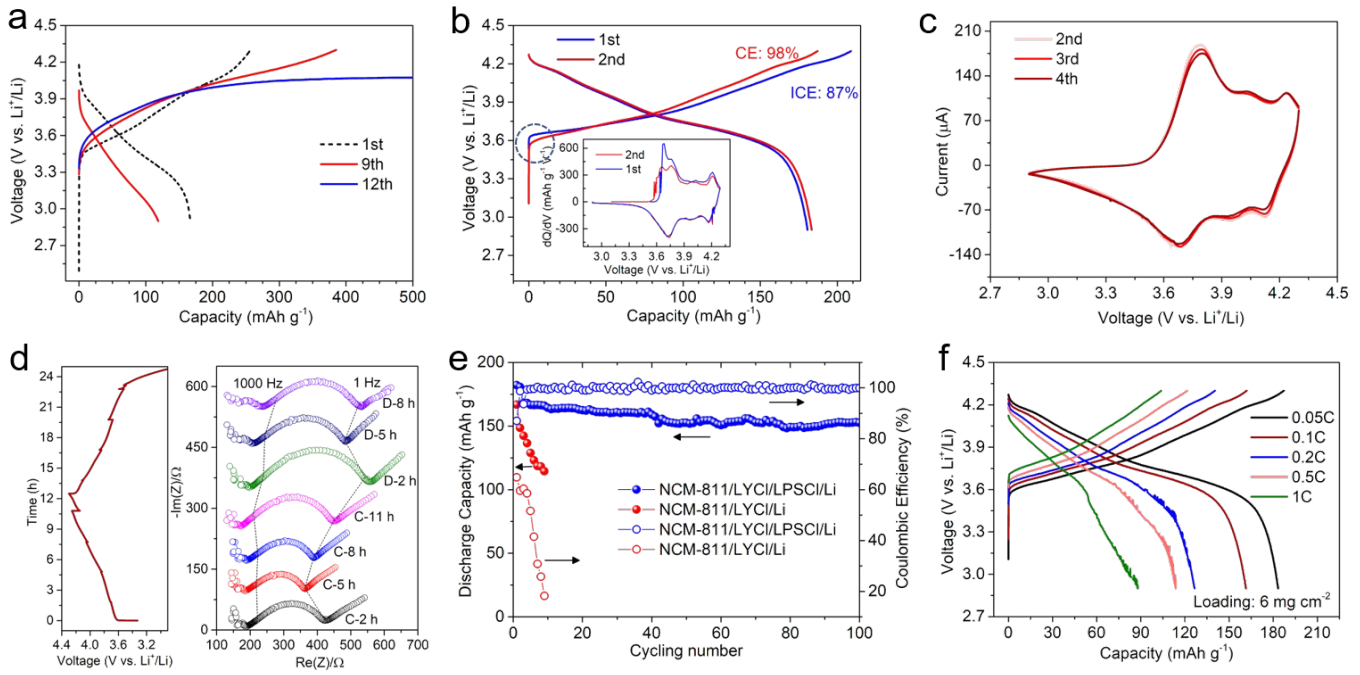

Fig. 5. a) Charge/discharge profiles of NCM-811/LYCl/Li cell at 0.1 mA cm^{-2}. Electrochemical performance of NCM-811/LYCl/LPSCl/Li cell: b) initial two charge/discharge profiles at 0.1 mA cm^{-2} (corresponding dQ/dV curves shown insert); c) CV profiles at 0.02 mV s^{-1}; d) impedance evolution during one charge/discharge cycle. e) cycling performance at 0.1 mA cm^{-2}; f) rate capability from 0.1 C to 1 C.

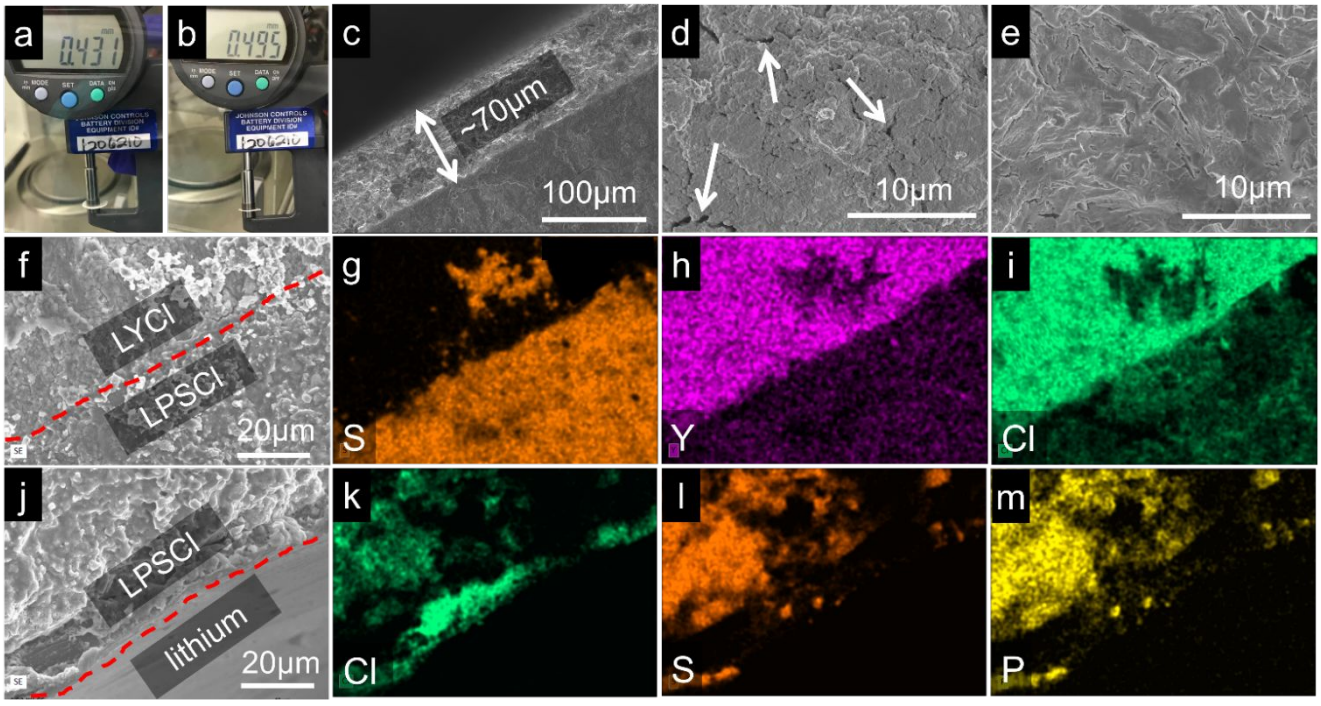

Fig. 6. Thickness measurement of the cold pressed a) LYCl pallet and b) LPSCl-LYCl pallet before cycling; after cycling: c) cross-sectional SEM image of the LPSCl-LYCl layer, top-view SEM images of d) LYCl surface and e) LPSCl surface; f) cross-sectional SEM image and g-i) elemental mapping analysis of the LYCl/LPSCl interface; j) cross-sectional SEM image and k-m) elemental mapping analysis of the LPSCl/lithium interface.

the three-phase transition process of NCM-811 material can be clearly observed from dQ/dV curves (insert Fig. 5b) and CV profiles (Fig. 5c).[39] The EIS evolution of full cell during one charge/discharge cycle (Fig. 5d) validates high interfacial stability of both LYCl/NCM-811 interface and LPSCl/Li interface. The full cell displayed stable cycling with a capacity retention of 91 % and a high CE of 99.7 % after 100 cycles (Fig. 5e). Table S2 listed the reported cycling performance of sulfide- and halide-based full cells based on high-Ni layered oxide cathodes. Our work displayed one of the highest initial CE and capacity retention among other works. Fig. 5f displayed the rate capability and a reversible discharge capacity of 90 mAh g^{-1} was achieved at 1C rate.

3.4 Investigation on the interface after cycling

The thickness of LYCl pallet and LYCl/LPSCl pallet before cycling is measured to be ~431 µm (Fig. 6a) and ~495 µm (Fig. 6b), respectively. Thus, the LPSCl layer can be roughly estimated as ~64 µm. According to the cross- sectional SEM image shown in Fig. 6c, after cycling, the thickness of LPSCl is about 70 µm, which is almost the same compared to before cycling. As indicated in Fig. 6d, the surface morphology of LYCl shows clear microcracks after cycling. By contrast, the LPSCl surface (Fig. 6e) is much smoother and exhibits no cracks throughout cycling, proved to be a good buffer layer. This should be ascribed to the ductile nature of sulfides, which can withstand higher local strain compared to halide electrolytes. Moreover, the intactness of LPSCl layer also indicates the decomposition reaction at the LPSCl/Li interface is well constrained, reflecting a self-limiting nature. As shown in Fig. 6f-i, a larger view of the LYCl/LPSCl interface after cycling is studied by SEM-EDS analysis. A clear transition region is presented by the distinguished difference of element distribution of sulfur, yttrium, and chloride (please ignore the small region in the upper middle area caused by powder contamination during sample preparation process). This unveils no chemical reaction or elemental diffusion occurred at the LYCl/LPSCl interface during cycling. As shown in Fig. 6j-m, a distinct LPSCl/Li metal interface was maintained after cycling, with no lithium dendrites or decomposition-induced thick SEI formation.

4. Conclusions

This Contribution, for the first time, employ lithium metal as anode in halide-based all-solid-state batteries. Argyrodite is selected as protection layer, due to its capability to form kinetically stable SEI layer in contact with Li and also form good hetero contact with halide electrolyte. Symmetric solid-state cell shows low polarization overpotential over 1000 h and $LiNi_{0.8}Co_{0.1}Mn_{0.1}O_2$/Li full cell displayed remarkably improved Coulombic efficiency and cycling stability. In practice, this offers a universal strategy to apply the class of halide-based electrolytes in all-solid-state lithium batteries.

Conflicts of interest

There are no conflicts to declare.

Acknowledgements

We thank John Condon from UWM Machine Shop for manufacturing the dies for solid-state cells. Research reported in this publication was supported by the Assistant Secretary for Energy Efficiency and Renewable Energy, Office of Vehicle Technologies, under the Vehicle Technology Program, under Contract Number DE-SC0012704 (D.Y.Q).

Notes and references

1 J. Janek, W.G. Zeier, *Nature Energy* 2016, **1**, 16141.
2 Z. Zhang, Y. Shao, B. Lotsch, Y.-S. Hu, H. Li, J. Janek, L.F. Nazar, C.-W. Nan, J. Maier, M. Armand, L. Chen, *Energy & Environ. Sci.* 2018, **11**, 1945-1976.
3 J.C. Bachman, S. Muy, A. Grimaud, H.-H. Chang, N. Pour, S.F. Lux, O. Paschos, F. Maglia, S. Lupart, P. Lamp, L. Giordano, Y. Shao-Horn, *Chem. Rev.* 2016, **116**, 140-162.
4 T. Famprikis, P. Canepa, J.A. Dawson, M.S. Islam, C. Masquelier, *Nature Mater.* 2019, **18**, 1278-1291.
5 A. Banerjee, X. Wang, C. Fang, E.A. Wu, Y.S. Meng, *Chem. Rev.* 2020, **120**, 6878-6933.
6 Y. Kato, S. Hori, T. Saito, K. Suzuki, M. Hirayama, A. Mitsui, M. Yonemura, H. Iba, R. Kanno, *Nature Energy* 2016, **1**, 16030.
7 N. Kamaya, K. Homma, Y. Yamakawa, M. Hirayama, R. Kanno, M. Yonemura, T. Kamiyama, Y. Kato, S. Hama, K. Kawamoto, A. Mitsui, *Nature Mater.* 2011, **10**, 682-686.
8 N. Zhao, W. Khokhar, Z. Bi, C. Shi, X. Guo, L.-Z. Fan, C.-W. Nan, *Joule* 2019, **3**, 1190-1199.
9 C. Wang, K. Fu, S.P. Kammampata, D.W. McOwen, A.J. Samson, L. Zhang, G.T. Hitz, A.M. Nolan, E.D. Wachsman, Y. Mo, V. Thangadurai, L. Hu, *Chem. Rev.* 2020, **120**, 4257-4300.
10 M. Balaish, J.C. Gonzalez-Rosillo, K.J. Kim, Y. Zhu, Z.D. Hood, J.L.M. Rupp, *Nature Energy* 2021, **6**, 227-239.
11 Y. Zhu, Y. Mo, *Angew. Chem. Int. Ed.* 2020, **59**, 17472-17476.
12 Y. Xiao, Y. Wang, S.-H. Bo, J.C. Kim, L.J. Miara, G. Ceder, *Nature Rev. Mater*. 2020, **5**, 105-126.
13 Y. Zhu, X. He, Y. Mo, *ACS Appl. Mater. Interfaces* 2015, **7**, 23685-23693.
14 R. Chen, Q. Li, X. Yu, L. Chen, H. Li, *Chem. Rev.* 2020, **120**, 6820-6877.
15 X. Li, J. Liang, X. Yang, K.R. Adair, C. Wang, F. Zhao, X. Sun, *Energy & Environ. Sci.* 2020, **13**, 1429-1461.
16 T. Asano, A. Sakai, S. Ouchi, M. Sakaida, A. Miyazaki, S. Hasegawa, *Adv. Energy Mater.* 2018, **30**, 1803075.
17 R. Schlem, T. Bernges, C. Li, M.A. Kraft, N. Minafra, W.G. Zeier, *ACS Appl. Energy Mater.* 2020, **3**, 3684-3691.
18 H. Kwak, D. Han, J. Lyoo, J. Park, S.H. Jung, Y. Han, G. Kwon, H. Kim, S.-T. Hong, K.-W. Nam, Y.S. Jung, *Adv. Energy Mater.* 2021, **11**, 2003190.
19 R. Schlem, S. Muy, N. Prinz, A. Banik, Y. Shao-Horn, M. Zobel, W.G. Zeier, *Adv. Energy Mater.* 2020, **10**, 1903719.
20 S. Wang, Q. Bai, A.M. Nolan, Y. Liu, S. Gong, Q. Sun, Y. Mo, *Angew. Chem. Int. Ed.* 2019, **58**, 8039-8043.
21 L. Zhou, C.Y. Kwok, A. Shyamsunder, Q. Zhang, X. Wu, L.F. Nazar, *Energy & Environ. Sci.* 2020, **13**, 2056-2063.
22 X. Li, J. Liang, J. Luo, M. Norouzi Banis, C. Wang, W. Li, S. Deng, C. Yu, F. Zhao, Y. Hu, T.-K. Sham, L. Zhang, S. Zhao, S. Lu, H. Huang, R. Li, K.R. Adair, X. Sun, *Energy & Environ. Sci.* 2019, **12**, 2665-2671.
23 L. Riegger, R. Schlem, J. Sann, W.G. Zeier, J. Janek, *Angew. Chem. Int. Ed.* 2021, **133**, 6792-6797.
24 Y. Fu, C. Ma, *Sci China Mater.* http://doi.org/10.1007/s40843-020-1580-3.
25 Y.-G. Lee, S. Fujiki, C. Jung, N. Suzuki, N. Yashiro, R. Omoda, D.-S. Ko, T. Shiratsuchi, T. Sugimoto, S. Ryu, J.H. Ku, T. Watanabe,

Y. Park, Y. Aihara, D. Im, I.T. Han, *Nature Energy* 2020, **5**, 299-308.
26 T.K. Schwietert, V.A. Arszelewska, C. Wang, C. Yu, A. Vasileiadis, N.J.J. de Klerk, J. Hageman, T. Hupfer, I. Kerkamm, Y. Xu, E. van der Maas, E.M. Kelder, S. Ganapathy, M. Wagemaker, *Nature Mater.* 2020, **19**, 428-435.
27 L. Ye and X. Li, *Nature* 2021, **593**, 218–222.
28 S. Wenzel, S.J. Sedlmaier, C. Dietrich, W.G. Zeier, J. Janek, *Solid State Ion.* 2018, **318**, 102-112.
29 X. Ji, S. Hou, P. Wang, X. He, N. Piao, J. Chen, X. Fan, C. Wang, *Adv. Mater.* 2020, **32**, 2002741.
30 R. Xu, F. Han, X. Ji, X. Fan, J. Tu, C. Wang, *Nano Energy* 2018, **53**, 958-966.
31 Y. Gao, D. Wang, Y.C. Li, Z. Yu, T.E. Mallouk, D. Wang, *Angew. Chem. Int. Ed.* 2018, **57**, 13608-13612.
32 C. Yu, Y. Li, K.R. Adair, W. Li, K. Goubitz, Y. Zhao, M.J. Willans, M.A. Thijs, C. Wang, F. Zhao, Q. Sun, S. Deng, J. Liang, X. Li, R. Li, T.-K. Sham, H. Huang, S. Lu, S. Zhao, L. Zhang, L. van Eijck, Y. Huang, X. Sun, *Nano Energy* 2020, **77**, 105097.
33 J. Liang, X. Li, S. Wang, K.R. Adair, W. Li, Y. Zhao, C. Wang, Y. Hu, L. Zhang, S. Zhao, S. Lu, H. Huang, R. Li, Y. Mo, X. Sun, *J. Am. Chem. Soc.* 2020, **142**, 7012-7022.
34 C. Hänsel, P.V. Kumar, D. Kundu, *Chem. Mater.* 2020, **32**, 10501-10510.
35 K.B. Hatzell, X.C. Chen, C.L. Cobb, N.P. Dasgupta, M.B. Dixit, L.E. Marbella, M.T. McDowell, P.P. Mukherjee, A. Verma, V. Viswanathan, A.S. Westover, W.G. Zeier, *ACS Energy Lett.* 2020, **5**, 922-934.
36 T. Krauskopf, F.H. Richter, W.G. Zeier, J. Janek, *Chem. Rev.* 2020, **120**, 7745-7794.
37 J. Tippens, J.C. Miers, A. Afshar, J.A. Lewis, F.J.Q. Cortes, H. Qiao, T.S. Marchese, C.V. Di Leo, C. Saldana, M.T. McDowell, *ACS Energy Lett.* 2019, **4**, 1475-1483.
38 J. Kasemchainan, S. Zekoll, D. Spencer Jolly, Z. Ning, G.O. Hartley, J. Marrow, P.G. Bruce, *Nature Mater.* 2019, **18**, 1105-1111.
39 Z. Zhang, D. Chen, C. Chang, *RSC Adv.* 2017, **7**, 51721-51728.